Engineered Science
DOI: https://dx.doi.org/10.30919/es1912

Enriching Carbon Nanotubes in Poly (Arylene Ether Nitrile) Porous Films for Enhanced Electromagnetic Shielding Properties

Lingling Wang,[1] Xiaofei Zhao,[1] Yue Yu,[1] Xiufu Hua[1,2,3,*] and Renbo Wei[1,*]

Abstract

The microstructure of the composite materials and the content of conductive fillers play a decisive role in the electromagnetic shielding performance. Herein, by leveraging the dispersing effect of polyvinylpyrrolidone (PVP K30) and its interaction with carbon nanotubes (CNTs), porous films with uniformly enriched CNTs at the pore interface are fabricated, resulting in a conductive three-dimensional network structure. By controlling the mass ratio of PVP K30 to CNTs, the honeycomb pore morphology is adjusted while avoiding high-content CNTs agglomeration. This results in a uniform enrichment of CNTs at the interface of porous films, reducing the CNTs content required to construct a continuous conductive network. The synergistic effect of the uniform CNTs enrichment at the porous films interface and the honeycomb pore structure promotes multiple reflections and absorptions of incident electromagnetic waves. The porous films with enriched CNTs at the interface exhibit a total shielding performance of 26.5 dB at 8.2 GHz, with an absorption loss of 23.6 dB. It also achieves a high tensile strength of 9.6 MPa and an elongation at break of 104%. This study provides a new approach for effectively controlling honeycomb pore size while uniformly dispersing CNTs.

Keywords: Honeycomb pore; Interface; Enrichment; Synergistic effect.
Received: 01 September 2025; Revised: 16 November 2025; Accepted: 25 November 2025
Article type: Research article.

1. Introduction

In recent years, polymer composites have been widely studied because of their good processability,[1,2] corrosion resistance[3] and light weight,[4,5] and gradually become an ideal substitute for traditional electromagnetic interference shielding materials.[6-8] The microstructure of composite materials and the content of functional fillers play a decisive role,[9-11] in which the formation of continuous conductive network structure in polymer matrix is a necessary condition for conductive composite films to have excellent electromagnetic shielding performance.[12-14] Using a large number of interfaces provided by porous structures in polymer films,[15-17] constructing a continuous conductive network is helpful to increase the reflection times of electromagnetic waves,[18-20] thereby increasing the loss of electromagnetic waves,[21,22] achieving the effect of shielding electromagnetic waves,[23,24] and opening up the application of polymer porous films in the field of electromagnetic shielding.[25-27]

Poly(arylene ether nitrile) (PEN) as a new type of special functional polymer possesses unique molecular structure. The porous film prepared with PEN as the matrix has significant advantages such as adjustable pore structure, mechanical stability, high-temperature resistance, oxidation resistance and corrosion resistance, etc. In the previous research, PEN porous films with different pore structures have been prepared by wet phase inversion method[28,30] If conductive fillers can be introduced into the PEN porous films to form conductive networks,[31-33] electromagnetic interference shielding materials with light weight and outstanding flexibility can be obtained.[34,35] Up to now, carbon-based materials with different structures or functions have been selected to be added to polymer matrix as modified fillers to improve the conductivity of the system.[36-41] Among them, carbon nanotubes (CNTs) are often used as conductive fillers to increase the conductivity of materials because of their excellent conductivity.[42-44]

However, due to the inherent Van der Waals force, high specific surface area and aspect ratio,[45] CNTs are easy to agglomerate,[46,47] and the preparation and application of CNTs

[1]*Institute of Low-Carbon Technology Application, School of Chemical Engineering, Northwest University, Xi'an, Shaanxi, 710069, China*
[2]*Yangtze Delta Region Institute of Tsinghua University, Jiaxing, Zhejiang, 314006, China*
[3]*Shaanxi Hydrogen Energy Industry Development Co., Ltd, Yulin, Shannxi, 719054, China*
[*]*Email:* huaxf@nwu.edu.cn (Xiufu Hua),
weirb10@nwu.edu.cn (Renbo Wei)

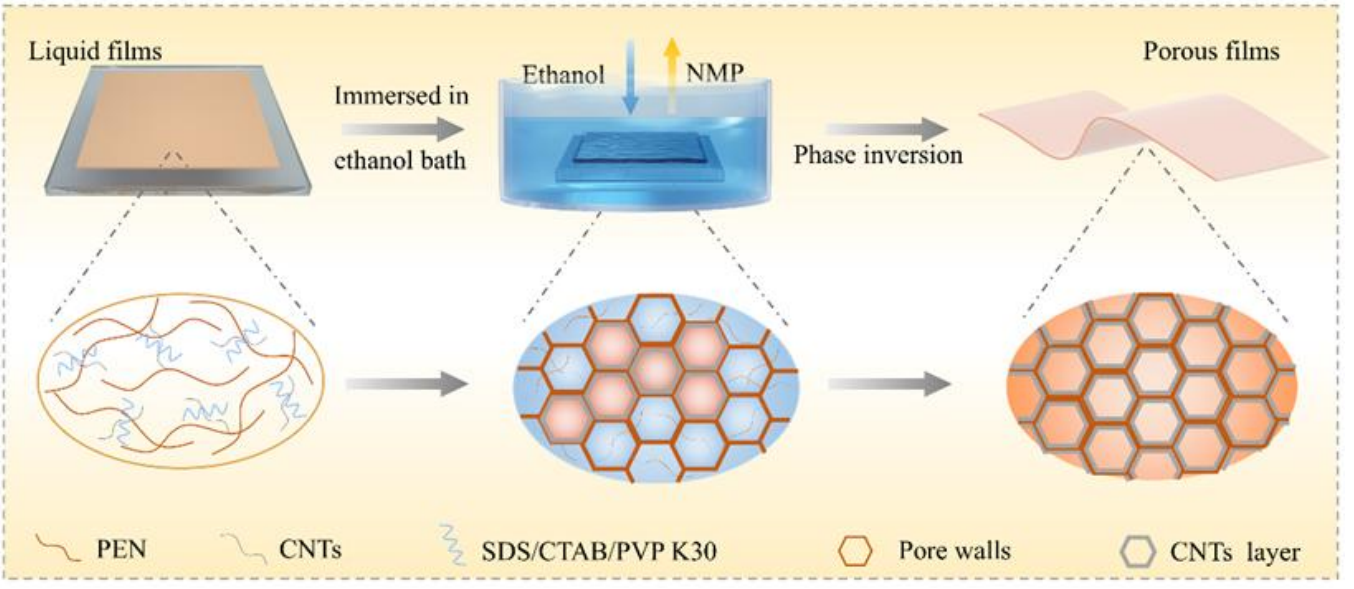

Fig. 1: Schematic diagram of fabrication procedure of porous films.

blended modified films are restricted by the poor compatibility and uneven distribution of CNTs when CNTs are directly blended with polymer matrix.[48,49] At the same time, the agglomeration of CNTs in the system increases the content of CNTs needed to build a continuous conductive network and seriously reduces the mechanical properties of composite material.[50,51] Surfactants are usually used to improve the dispersion of CNTs.[52] As a pore-forming agent with good hydrophilicity, polyvinylpyrrolidone (PVP) K30 can be physically and chemically grafted with the surfaces of various carbon-based materials through π-π bonds or hydrogen bonds, thus improving the dispersion stability of carbon-based materials in various matrixs.[53]

In this research, the dispersion effect of PVP K30 and its interaction with CNTs were used to promote the segregation of CNTs on the pore wall, thus preparing PEN porous films with uniformly enriched CNTs on the surface of pores, and obtaining a conductive three-dimensional network structure; By controlling the mass ratio of PVP K30 to CNTs and adjusting the honeycomb pore structure, the CNTs were uniformly enriched on the pore wall of the PEN porous film. The synergistic effects of uniform enrichment of CNTs and honeycomb pores on the structure and properties of PEN porous film were systematically studied, and its application in electromagnetic shielding was explored.

2. Experimental parts

2.1 Materials

The PEN was synthesized via a condensation polymerization reaction.[54,55] Biological reagent Pluronic F127 was purchased from Sigma-Aldrich. Carbon nanotubes were purchased from Beijing Deke Daojin Company, with a diameter of 60 nm and a length of 10-30 μm. Sodium dodecyl sulfate, cetyl trimethyl ammonium bromide, N-methylpyrrolidone and ethanol were acquired from Chengdu Kelong Factory. Polyvinyl Pyrrolidone was purchased from Shanghai Aladdin Biochemical Technology Co., Ltd.

2.2 Preparation of polyarylether nitrile film with CNTs enriched at interface

2.2.1 Preparation of polyarylether nitrile films directly introducing CNTs

A certain amount of carbon nanotubes (CNTs) was dispersed in N- methylpyrrolidone (NMP) solvent by ultrasonic treatment for 2 h to obtain CNTs/NMP solution. Afterwards, a certain amount of polyarylether nitrile (PEN) was added to the CNTs/NMP solution, where PEN/(PEN+NMP) was 10 wt%, and mechanical stirring at 300 r/min was applied, and ultrasonic stirring was continued for 1 h until the PEN was completely dissolved to obtain the CNTs/PEN/NMP solution. Then pour the solution obtained from the above preparation on one side of the glass plate, push out the 1000 μm liquid film from one side of the glass plate to the other side slowly and uniformly with a wet film preparator, and immerse it into an ethanol solidification bath at 25 ℃. After the liquid film was converted into a solid film, it was peeled off from the glass plate, after which it was continued to be immersed in ethanol for 48 h to obtain the CNTs/PEN wet-state film. The CNTs/PEN film was dried in an oven at 30 ℃ for 12 h, and the oven was naturally cooled to room temperature to obtain the CNTs/PEN composite film, named $F_{M\text{-}a}$, where M represents CNTs and a is the mass fraction of CNTs in the CNTs/PEN composite film, which are 0 wt%, 3 wt%, 6 wt%, 9 wt%, 12 wt% and 15 wt%, respectively.

2.2.2 Preparation of PEN porous films incorporating surfactants and CNTs

As shown in Fig. 1, a certain amount of CNTs and polyvinylpyrrolidone (PVP K30) were dispersed into the NMP solvent by ultrasonication for 2 h. After that, PEN was added

to the PVP K30/CNTs/NMP solution by mechanical stirring at 300 r/min, in which the PEN/(PEN+NMP) was 10 wt%, and ultrasonic stirring was continued for 1 h until the PEN was completely dissolved to obtain the PVP K30/CNTs/PEN/NMP solution. Then the solution obtained from the above preparation was poured on one side of the glass plate, and a liquid film of 1000 μm was pushed out slowly and uniformly from one side of the template to the other side with a wet film preparator, and then immersed into an ethanol solidification bath at 25 ℃, and then after the liquid film was transformed into a solid film, it was peeled off from the glass plate, and then continued to be immersed in ethanol coagulation for 48 h, and then a wet film of PVP K30/CNTs/PEN was obtained.

The PVP K30/CNTs/PEN film was dried at 30 ℃ for 12 h, and the oven was naturally cooled to room temperature to obtain PVP K30/CNTs/PEN composite film, named $F_{M\text{-}a\text{-}P\text{-}b}$, where M stands for CNTs, a is the mass fraction of CNTs, which is denoted as CNTs/(PEN+CNTs+PVP K30), and P stands for PVP K30, and b is the mass fraction of PVP K30, which is denoted as PVP K30/(PEN+CNTs+PVP K30). Different PVP K30/CNTs/PEN composite films were obtained by varying the amount of CNTs and PVP K30. As a comparison, the mass fraction of CNTs was controlled to be 12 wt%, and at the same time, the PVP K30 in the above operation was changed to SDS or CTAB, and its mass fraction in the film was controlled to be 6 wt%, and the other operating conditions remained unchanged, and the PEN porous film obtained was named as $F_{M\text{-}12\text{-}X\text{-}6}$, with X standing for surfactant, and S, C, respectively, and correspondingly was named as $F_{M\text{-}12\text{-}S\text{-}6}$, $F_{M\text{-}12\text{-}C\text{-}6}$, wherein S stood for SDS and C stood for CTAB.

2.3 Characterization methods and instrumentation

The micromorphology of cross section of the porous films was characterized using a scanning electron microscope (SEM) model JSM-6490LV produced by JEOL Ltd. The volume resistivity of the films was measured on a four-point probe resistivity tester (Signatone, USA) using the standard four-probe technique (RTS-8, Guangzhou Four-Point Probe Technology Co., Ltd., China). The mechanical properties of the porous films were tested using a SANS CMT6104 microcomputer-controlled electronic universal testing machine produced by Shenzhen Xinsansi Company. The third part of the ISO 527 international standard (ISO 527-3) was adopted for testing the mechanical properties of porous films, and the rising rate was set to 5 mm/min. The electromagnetic interference shielding performance of porous film was measured using a PNA Network Analyzer model N5224B，the measurement frequency range is 8.2 to 12.4 GHz (X-band), and the scattering parameters (S11 and S21) in the X-band are recorded, and the reflection coefficients (R), transmission coefficients (T), absorption coefficients (A), reflection shielding (SE_R), absorption shielding (SE_A), total electromagnetic shielding (SE_T), electromagnetic shielding efficiency (E) are calculated using Eq. (1-7), respectively:

$$R = |S_{11}|^2 \tag{1}$$

$$T = |S_{21}|^2 \tag{2}$$

$$A = 1 - R - T \tag{3}$$

$$SE_R = -10\log(1 - R) \tag{4}$$

$$SE_A = -10\log\left(\frac{T}{1 - R}\right) \tag{5}$$

$$SE_T = SE_A + SE_R + SE_M \tag{6}$$

$$E = 100 - \left(\frac{1}{10^{\frac{10}{SE}}}\right) \times 100 \tag{7}$$

3. Results and discussion

Constructing a continuous conductive network structure in porous films helps to enhance the electromagnetic shielding properties of materials. Therefore, in this research, three different types of surfactants were selected, namely cationic surfactant CTAB, anionic surfactant SDS, and nonionic polymer surfactant PVP K30. At the same time, the mass fraction of CNTs was fixed at 12 wt%, and the mass fraction of surfactant was 6 wt%. CNTs were introduced into PEN porous films by wet phase inversion method. The effects of different types of surfactants on the distribution of CNTs in the porous film $F_{M\text{-}12\text{-}X\text{-}6}$ with CNTs enriched at the interface and its effect on the pore structure and properties of the film were investigated.

The binding energy was calculated by Materials Studio to characterize the interaction, which assists in explaining the way in which CNTs are enriched in the pore wall of the porous films, as shown in Figure 2a~2c. The binding energy between SDS and CNTs was calculated to be -215.9 kJ/mol, CTAB and CNTs was -254.2 kJ/mol, and PVP K30 and CNTs was -1757.76 kJ/mol. The above calculation results show that the interaction between PVP K30 and CNTs is much larger than that between SDS and CNTs and between CTAB and CNTs. Fig. 2d-f is the SEM image of the cross-section morphology of $F_{M\text{-}12\text{-}X\text{-}6}$. Fig. 2d, 2e, 2j and 2h are the SEM images of the cross-section morphology of $F_{M\text{-}12\text{-}S\text{-}6}$ and $F_{M\text{-}12\text{-}C\text{-}6}$ and pore size distribution. The pore structure of $F_{M\text{-}12\text{-}S\text{-}6}$ and $F_{M\text{-}12\text{-}C\text{-}6}$ maintained the honeycomb pore of pure PEN porous film. The size of the honeycomb pores of $F_{M\text{-}12\text{-}S\text{-}6}$ and $F_{M\text{-}12\text{-}C\text{-}6}$ is larger than that of $F_{M\text{-}12}$, but the size distribution is not uniform. The increase of pore size is mainly due to the hydrophilicity of SDS or CTAB and the agglomeration of CNTs.

Fig. 2f are the SEM images of the cross-section morphology of $F_{M\text{-}12\text{-}P\text{-}6}$. With the addition of PVP K30, the

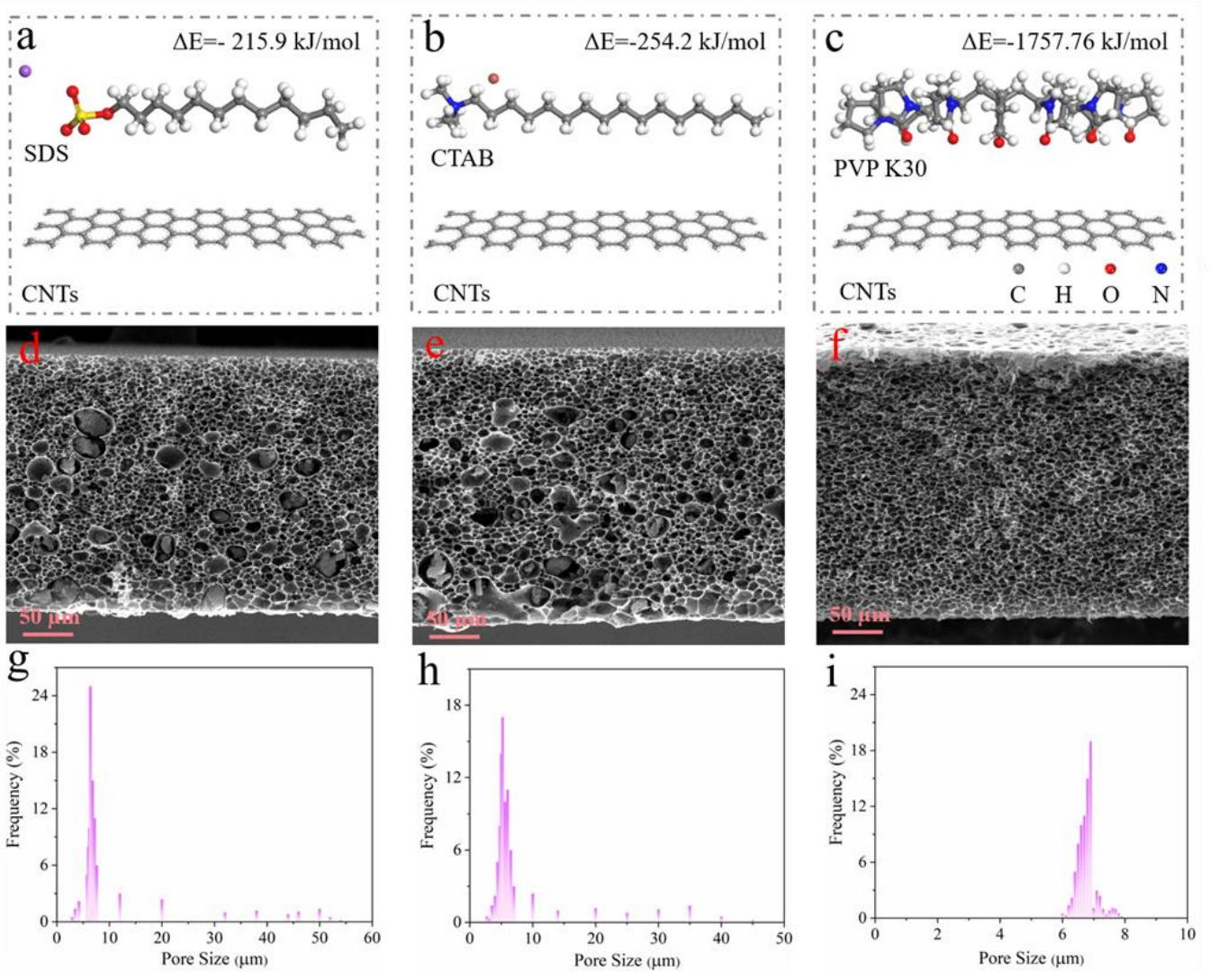

Fig. 2: The interaction energies between SDS (a), CTAB (b), PVP K30 (c) and CNTs calculated via DFT method; SEM images of the cross-section morphology of porous films (d) $F_{M\text{-}12\text{-}S\text{-}6}$, (e) $F_{M\text{-}12\text{-}C\text{-}6}$, (f) $F_{M\text{-}12\text{-}P\text{-}6}$ enriched with CNTs at the interface; The pore size percentage of $F_{M\text{-}12\text{-}S\text{-}6}$ (j), $F_{M\text{-}12\text{-}C\text{-}6}$ (h), and $F_{M\text{-}12\text{-}P\text{-}6}$ (i).

pore structure of $F_{M\text{-}12\text{-}P\text{-}6}$ maintained the honeycomb pore structure of pure PEN porous film. Compared with the size of the $F_{M\text{-}12}$ pore without PVP K30, the size of the honeycomb pore in $F_{M\text{-}12\text{-}P\text{-}6}$ increased as a whole. The increase of pore size is due to the hydrophilicity of PVP K30 acting as porogens. The addition of hydrophilic PVP K30 increases the mass transfer rate in the formation process of porous film and increases the pore size. Different from the addition of SDS and CTAB, the distribution of CNTs in $F_{M\text{-}12\text{-}P\text{-}6}$ was uniformly dispersed due to the addition of PVP K30, and no hydrangea-like agglomerated CNTs and the junctions were found in the honeycomb pores of $F_{M\text{-}12\text{-}P\text{-}6}$. There were no satin-like CNTs wrapped or interspersed in the pore wall. CNTs were distributed in a single filament on the honeycomb pore wall. CNTs on the surface of a single pore wall overlapped with each other, and CNTs between pores also overlapped. CNTs showed a spider web-like enrichment on the surface of the honeycomb pore wall. In addition, the honeycomb pore size in $F_{M\text{-}12\text{-}P\text{-}6}$ is uniform, at 5.2±0.7 μm as shown in Fig. 2i.

The above results showed that both CTAB and SDS failed to achieve the effect of promoting the uniform enrichment of CNTs in the inner pore wall, and did not play an effective role in improving the agglomeration of CNTs, but both increased the size of honeycomb pores to a certain extent. PVP K30 effectively promotes the uniform enrichment of CNTs in the inner pore wall, which plays an effective role in improving the agglomeration of CNTs, and increases the size of honeycomb pores. The uniform enrichment of CNTs in the internal pore wall of porous films is due to the strong interaction between PVP K30 and CNTs and the migration of PVP K30 to the interface during the film formation process. The five-membered ring structure of pyrrolidone in PVP K30 contributes to the formation of π-π conjugation with π electrons in CNTs, thereby increasing its adsorption on the

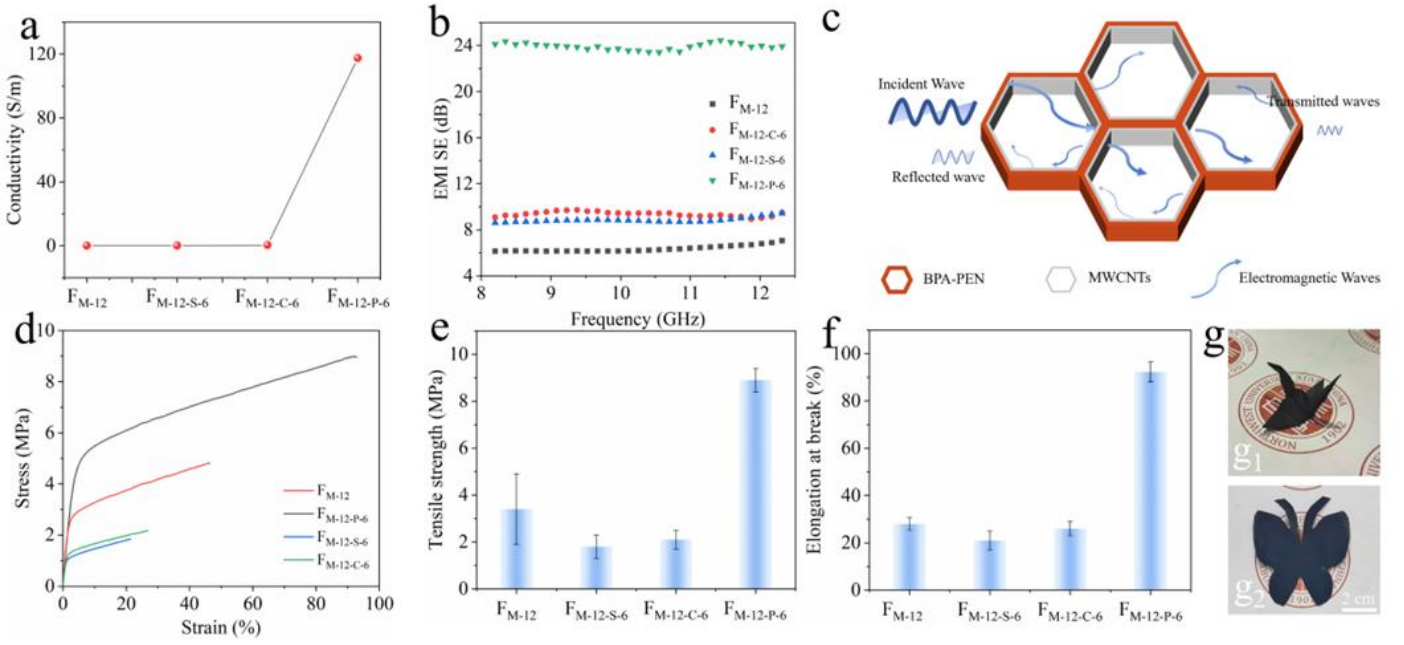

Fig. 3: (a) The conductivity of polyarylether-nitrile porous film $F_{M\text{-}12\text{-}X\text{-}6}$; (b) The electromagnetic shielding performance of $F_{M\text{-}12\text{-}X\text{-}6}$ as a function of frequency; (c) The electromagnetic shielding mechanism diagram of $F_{M\text{-}12\text{-}X\text{-}6}$; (d) The stress-strain curves (e), tensile strength (f) and physical pictures (g) of $F_{M\text{-}12\text{-}X\text{-}6}$.

surface of CNTs. After the adsorption of PVP K30, the long chain structure of PVP K30 can play a steric hindrance to hinder the agglomeration and entanglement between CNTs. During the film formation process, PVP K30 on the surface of CNTs tends to migrate to the interface between the casting solution and coagulation bath, driving the uniform enrichment of CNTs on pore walls.

After studying the cross-section structure of $F_{M\text{-}12\text{-}X\text{-}6}$, the effects of different surfactants on the conductivity of $F_{M\text{-}12\text{-}X\text{-}6}$ were tested. As shown in Fig. 3a, compared with the conductivity of $F_{M\text{-}12}$ without surfactant, the conductivity of $F_{M\text{-}12\text{-}S\text{-}6}$ and $F_{M\text{-}12\text{-}C\text{-}6}$ increased from 0.09 S/m of FM-12 to 0.11 S/m and 0.48 S/m, respectively; Compared with the above two surfactants, the conductivity of FM-12-P-6 increased significantly to 117.5 S/m. The above results show that the addition of SDS and CTAB can change the agglomeration behavior of CNTs in the polymer matrix, but it is not suitable for the wet phase inversion process, although it has been reported in the literature that it can significantly improve the agglomeration behavior of CNTs in the polymer matrix in the dense film; PVP K30 is suitable for wet phase inversion process to improve the dispersion performance of CNTs in porous film, which promotes the uniform distribution of CNTs in $F_{M\text{-}12\text{-}P\text{-}6}$ and the overlap between CNTs constitutes an effective conductive path.

The electromagnetic interference shielding effectiveness (EMI SE) value of the $F_{M\text{-}12\text{-}X\text{-}6}$ was measured in the microwave frequency range of 8.2-12.4 GHz. When the content of CNTs is 12 wt%, the EMI SE of $F_{M\text{-}12\text{-}X\text{-}6}$ with interface enrichment of CNTs is shown in Fig. 3b. Compared with the EMI SE of $F_{M\text{-}12}$ at 8.2 GHz, the EMI SE of $F_{M\text{-}12\text{-}S\text{-}6}$ and $F_{M\text{-}12\text{-}C\text{-}6}$ increased to 8.6 dB and 9.1 dB at 8.2 GHz. However, the range of improvement is limited and does not meet the application requirements. When 6 wt% PVP K30 was added, the EMI SE of $F_{M\text{-}12\text{-}P\text{-}6}$ was improved to 24.2 dB at 8.2 GHz, which met the effective EMI SE value required for practical applications. The satisfactory EMI SE value of FM-12-P-6 is beneficial to the uniform enrichment of CNTs on the honeycomb pore wall and the overlapping of CNTs to construct an effective conductive network path. Due to the honeycomb structure of the conductive network, the interface of more conductive pores in $F_{M\text{-}12\text{-}P\text{-}6}$ promotes the multiple reflection of electromagnetic waves in the honeycomb conductive network structure, which is helpful to realize the effective dissipation of electromagnetic waves.

Fig. 3c is the electromagnetic shielding mechanism diagram of $F_{M\text{-}12\text{-}P\text{-}6}$ with CNTs-enriched interface. The cellular pore structure of $F_{M\text{-}12\text{-}P\text{-}6}$ with an interface rich in CNTs can be represented by a hexagon, and the CNTs with an interface rich in CNTs form a conductive layer of CNTs on the pore walls of these cellular pores. There are three possible attenuation mechanisms for the electromagnetic wave attenuation of $F_{M\text{-}12\text{-}P\text{-}6}$, namely, the reflection shielding of the electromagnetic wave by the CNTs layer enriched at the interface of $F_{M\text{-}12\text{-}P\text{-}6}$, the absorption of the electromagnetic wave by the CNTs layer in $F_{M\text{-}12\text{-}P\text{-}6}$, and the multiple

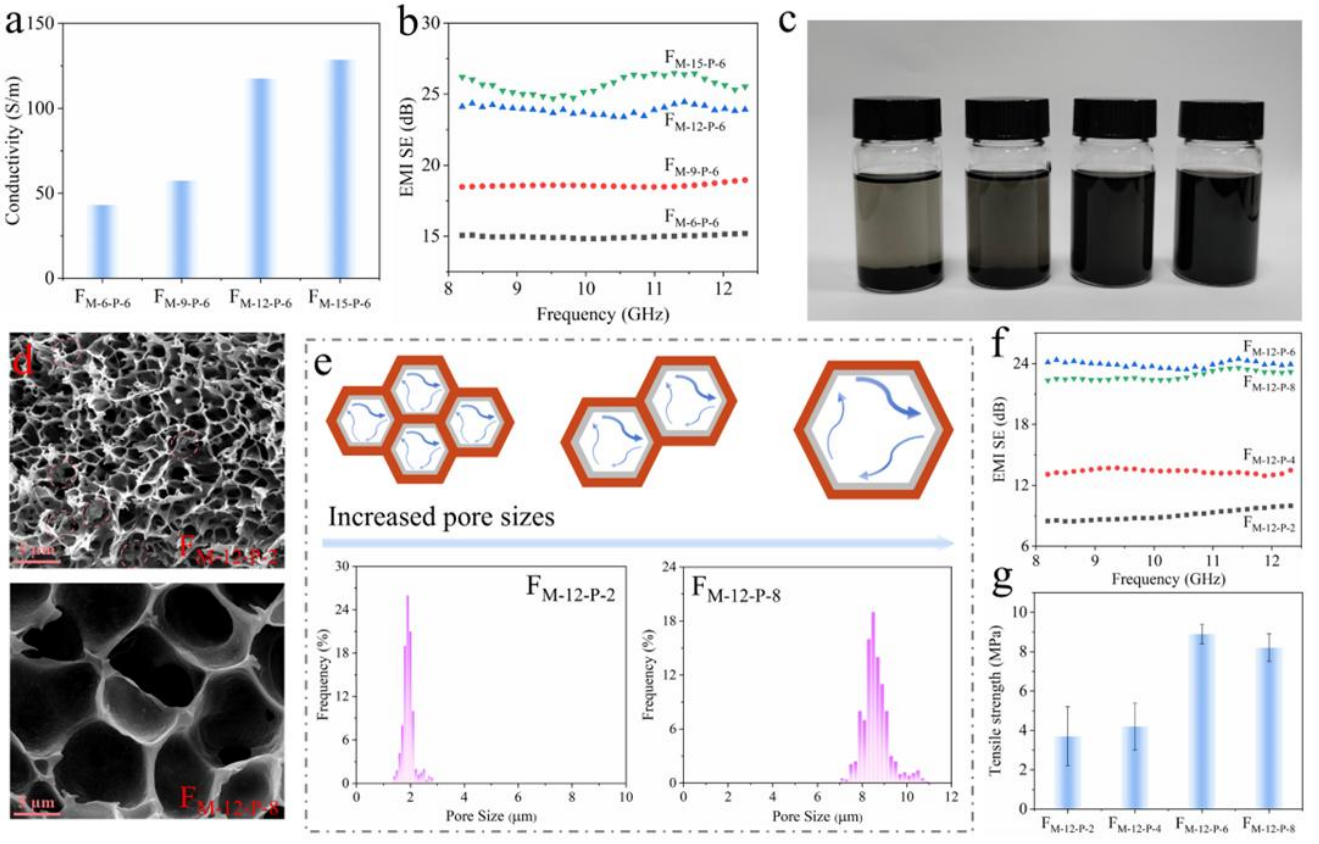

Fig. 4: (a) The conductivity of $F_{M\text{-}a\text{-}P\text{-}6}$; (b) The electromagnetic shielding performance of $F_{M\text{-}a\text{-}P\text{-}6}$ as a function of frequency; (c) The static diagram of $F_{M\text{-}a\text{-}P\text{-}6}$ solution; (d) SEM images of the cross-section morphology of $F_{M\text{-}12\text{-}P\text{-}b}$. (e) The pore size percentage and electromagnetic shielding mechanism of $F_{M\text{-}12\text{-}P\text{-}b}$; (f) The electromagnetic shielding performance of $F_{M\text{-}12\text{-}P\text{-}b}$ as a function of frequency; (g) Tensile strength of $F_{M\text{-}12\text{-}P\text{-}b}$.

reflections of the electromagnetic wave inside $F_{M\text{-}12\text{-}P\text{-}6}$ to achieve the attenuation and dissipation of electromagnetic wave energy, mainly related to the reflection of moving charge carriers, electric dipoles and various surfaces or interfaces.

The mechanical properties of $F_{M\text{-}12\text{-}X\text{-}6}$ prepared by adding different kinds of surfactants are shown in Fig. 3d - 3g. Compared with the mechanical properties of $F_{M\text{-}12}$, the mechanical properties of $F_{M\text{-}12\text{-}S\text{-}6}$ and $F_{M\text{-}12\text{-}C\text{-}6}$ were significantly reduced. The tensile strength decreased from 3.4 MPa to 1.8 MPa and 2.1 MPa, respectively, and the elongation at break decreased from 28.5 % to 21.4 % and 26.7 %. The change of mechanical properties of $F_{M\text{-}12\text{-}S\text{-}6}$ and $F_{M\text{-}12\text{-}C\text{-}6}$ is mainly due to the aggregation of CNTs and the change of pore structure of porous films. Due to the addition of SDS and CTAB did not improve the agglomeration of CNTs, while increasing the size of the honeycomb pores. The serious agglomeration of CNTs reduces the effective connection between honeycomb pores and reduces the transmission channel between stresses. Compared with the mechanical properties of $F_{M\text{-}12}$, the mechanical properties of $F_{M\text{-}12\text{-}P\text{-}6}$ increased significantly. The tensile strength of $F_{M\text{-}12\text{-}P\text{-}6}$ increased to 8.9 MPa, and the elongation at break increased to 92.3 %. The improvement of mechanical properties of $F_{M\text{-}12\text{-}P\text{-}6}$ is mainly due to the change of honeycomb structure and CNTs distribution.

Fig. S1 shows the SEM image of the cross-section morphology of $F_{M\text{-}a\text{-}P\text{-}6}$. Due to the addition of PVP K30, the cross section of $F_{M\text{-}a\text{-}P\text{-}6}$ was honeycomb pore structure. Compared with $F_{M\text{-}6}$ without PVP K30, the honeycomb pore size of $F_{M\text{-}a\text{-}P\text{-}6}$ with quantitative PVP K30 increased. The honeycomb pore size of $F_{M\text{-}a\text{-}P\text{-}6}$ is larger than that of $F_{M\text{-}6}$ because of the hydrophilicity of PVP K30, and the addition of PVP K30 increases the mass transfer rate in the process of phase transformation, thus increasing the pore size. With the increase of CNTs content, the honeycomb pore size of $F_{M\text{-}a\text{-}P\text{-}6}$ decreases slightly. The reason is that the amount of PVP K30 added is certain. The promotion effect of PVP K30 on the phase inversion mass transfer rate is similar, and pore sizes is increased to the same extent. The addition of CNTs increases the viscosity of casting solution and reduces the mass transfer rate of phase inversion, which hinders the mutual diffusion between the casting solution and coagulation bath.

As shown in Fig. 4a, with the increase of CNTs content from 6 wt% to 15 wt%, the electrical conductivity of $F_{M\text{-}a\text{-}P\text{-}6}$ gradually increased from 43.1 S/m of $F_{M\text{-}6\text{-}P\text{-}6}$ to 128.6 S/m of $F_{M\text{-}15\text{-}P\text{-}6}$. On the one hand, the increase of conductivity of $F_{M\text{-}a\text{-}P\text{-}6}$ is due to the good conductivity of CNTs, on the other hand, it is also related to the uniform distribution of CNTs and

whether a conductive network can be constructed. The above results show that with the addition of 6 wt% PVP K30, only 6 wt% CNTs are needed to construct a conductive network structure in $F_{M\text{-}a\text{-}P\text{-}6}$, forming an effective conductive path, which significantly increases the conductivity of $F_{M\text{-}a\text{-}P\text{-}6}$, while more CNTs can further promote the formation of conductive network in $F_{M\text{-}a\text{-}P\text{-}6}$.

Fig. 4b shows the influence of different CNTs content on the electromagnetic shielding performance of $F_{M\text{-}a\text{-}P\text{-}6}$ with 6 wt% PVP K30. With the frequency rising from 8.2 GHz to 12.4 GHz, only $F_{M\text{-}15\text{-}P\text{-}6}$ has maximum and minimum values, but the electromagnetic shielding performance is not more than 3 dB. With the increase of CNTs content from 6 wt% to 15 wt%, the electromagnetic shielding performance of $F_{M\text{-}a\text{-}P\text{-}6}$ at 8.2 GHz gradually increased from 16.9 dB of $F_{M\text{-}6\text{-}P\text{-}6}$ to 29.5 dB of $F_{M\text{-}15\text{-}P\text{-}6}$. The conductive network in $F_{M\text{-}a\text{-}P\text{-}6}$ presents a honeycomb structure, which promotes the electromagnetic wave to reflect back and forth in the honeycomb conductive network structure and realizes the effective dissipation of electromagnetic wave. The electromagnetic shielding performance of $F_{M\text{-}a\text{-}P\text{-}6}$ increases with the increase of CNTs content, which is mainly due to the enhanced conductivity of high content of CNTs, the uniform dispersion of CNTs on the honeycomb pore wall and the significantly increased conductivity of effective conductive network paths.

Fig. S2 shows the electromagnetic shielding parameter values of $F_{M\text{-}a\text{-}P\text{-}6}$. The results show that the absorption shielding SE_A value of $F_{M\text{-}a\text{-}P\text{-}b}$ is higher than the reflection shielding SE_R value, no matter how the CNTs content of $F_{M\text{-}a\text{-}P\text{-}b}$ and the size of honeycomb pores change, indicating that $F_{M\text{-}a\text{-}P\text{-}6}$ with honeycomb conductive network structure is an electromagnetic shielding mechanism based on absorption mechanism. Taking $F_{M\text{-}12\text{-}P\text{-}6}$ as an example, when the content of CNTs was 12 wt%, the SE_T, SE_A and SE_R values of $F_{M\text{-}12\text{-}P\text{-}6}$ were 24.1 dB, 22.1 dB and 2.0 dB, respectively. The electromagnetic shielding parameter value of $F_{M\text{-}a\text{-}P\text{-}6}$ increases with the increase of CNTs content, which can be attributed to the sawtooth reflection mechanism caused by the honeycomb pore wall enriched with CNTs in $F_{M\text{-}a\text{-}P\text{-}6}$, which will cause more electromagnetic waves to continuously reflect and absorb in the honeycomb pores.

Fig. S3 show the tensile strength and elongation at break of $F_{M\text{-}a\text{-}P\text{-}6}$ prepared by adding 6 wt% PVP K30 with different contents of CNTs. The results showed that when the content of PVP K30 was fixed at 6 wt%, the tensile strength of $F_{M\text{-}a\text{-}P\text{-}6}$ gradually increased and the elongation at break gradually decreased with the increase of CNTs content from 6 wt% to 15 wt%.The tensile strength of $F_{M\text{-}a\text{-}P\text{-}6}$ increased from 7.5 MPa of $F_{M\text{-}6\text{-}P\text{-}6}$ to 9.6 MPa of $F_{M\text{-}15\text{-}P\text{-}6}$, and the elongation at break decreased from 103.7 % of $F_{M\text{-}6\text{-}P\text{-}6}$ to 88.1 % of $F_{M\text{-}15\text{-}P\text{-}6}$. The change of mechanical properties of $F_{M\text{-}a\text{-}P\text{-}6}$ is mainly due to the change of CNTs content and the resulting change of honeycomb pore structure of $F_{M\text{-}a\text{-}P\text{-}6}$.

The static diagram at Fig. 4c shows the effect of PVP K30 content on the distribution of CNTs when the CNTs content was fixed at 12 wt%. Fig. 4d and Fig. S5 is the SEM image of the cross-section morphology of $F_{M\text{-}12\text{-}P\text{-}b}$, in which $F_{M\text{-}12\text{-}P\text{-}b}$ with different PVP K30 contents all show a honeycomb pore structure. PVP K30 can improve the dispersion state of CNTs in the porous film, and there is an optimal ratio between CNTs and PVP K30. When the mass ratio of PVP K30 to CNTs is less than 1: 2, the increase of PVP K30 content can promote the agglomeration of CNTs, effectively promote the uniform enrichment of CNTs on the pore wall of porous films, and the agglomeration of CNTs in the porous films is gradually reduced. When the mass ratio of PVP K30 to CNTs reached 2:1, the CNTs showed a spider web-like enrichment on the entire honeycomb pore wall. In addition, the honeycomb pore size of $F_{M\text{-}12\text{-}P\text{-}b}$ increased with the increase of PVP K30 content, as shown in Fig. 4e. The increase of honeycomb pore size is mainly due to the increase of the mass transfer rate in the formation process of porous film $F_{M\text{-}12\text{-}P\text{-}b}$.

The effect of different contents of PVP K30 on the conductivity of $F_{M\text{-}12\text{-}P\text{-}b}$ was studied when the content of CNTs was fixed at 12 wt%. As shown in Fig. S4, when the CNTs content is fixed at 12 wt%, as the PVP K30 content increases from 2 wt% to 4wt%, the conductivity of $F_{M\text{-}12\text{-}P\text{-}b}$ increases from 0.09 S/m of $F_{M\text{-}12\text{-}P\text{-}2}$ to 0.83 S / m of $F_{M\text{-}12\text{-}P\text{-}4}$. When the content of PVP K30 continued to increase to 8 wt%, the conductivity of $F_{M\text{-}12\text{-}P\text{-}8}$ only increased to 117.7 S/m, and there was no significant increase compared with $F_{M\text{-}12\text{-}P\text{-}6}$. The remarkable change of conductivity of $F_{M\text{-}12\text{-}P\text{-}b}$ is mainly due to the uniform enrichment of CNTs in the honeycomb wall of porous film. When the content of PVP K30 is 6 wt% and 8 wt%, CNTs are uniformly enriched on the honeycomb pore wall, forming a spider-like mesh of overlapping CNTs layers. Because the content of CNTs is fixed at 12 wt%, and the conductive filler that can form a continuous conductive path is certain, the conductivity of $F_{M\text{-}12\text{-}P\text{-}b}$ no longer increases with the increase of PVP K30 content, but the honeycomb pore size has little influence on the conductivity of $F_{M\text{-}12\text{-}P\text{-}b}$.

Fig. 4f shows the variation curve of electromagnetic shielding performance with frequency of porous film $F_{M\text{-}12\text{-}P\text{-}b}$. The results show that the electromagnetic shielding performance of $F_{M\text{-}12\text{-}P\text{-}b}$ first increases and then decreases with the increase of PVP K30 content. When the content of CNTs is fixed at 12 wt%, with the content of PVP K30 increasing from 2 wt% to 8 wt%, the electromagnetic shielding performance of $F_{M\text{-}12\text{-}P\text{-}b}$ at 8.2 GHz increases from 8.5 dB of $F_{M\text{-}12\text{-}P\text{-}2}$ to 24.1 dB of $F_{M\text{-}12\text{-}P\text{-}6}$, and then begins to decline to 22.3 dB $F_{M\text{-}12\text{-}p\text{-}8}$. The effective electromagnetic shielding of $F_{M\text{-}12\text{-}P\text{-}b}$ is beneficial to the uniform enrichment of CNTs on the honeycomb pore wall and the effective conductive network path constructed by the overlapping of CNTs. Because the conductive network presents a honeycomb structure, electromagnetic waves are reflected back and forth in the honeycomb conductive network structure, which is helpful to realize the effective dissipation of electromagnetic waves. The electromagnetic shielding performance of porous film $F_{M\text{-}12\text{-}P\text{-}}$

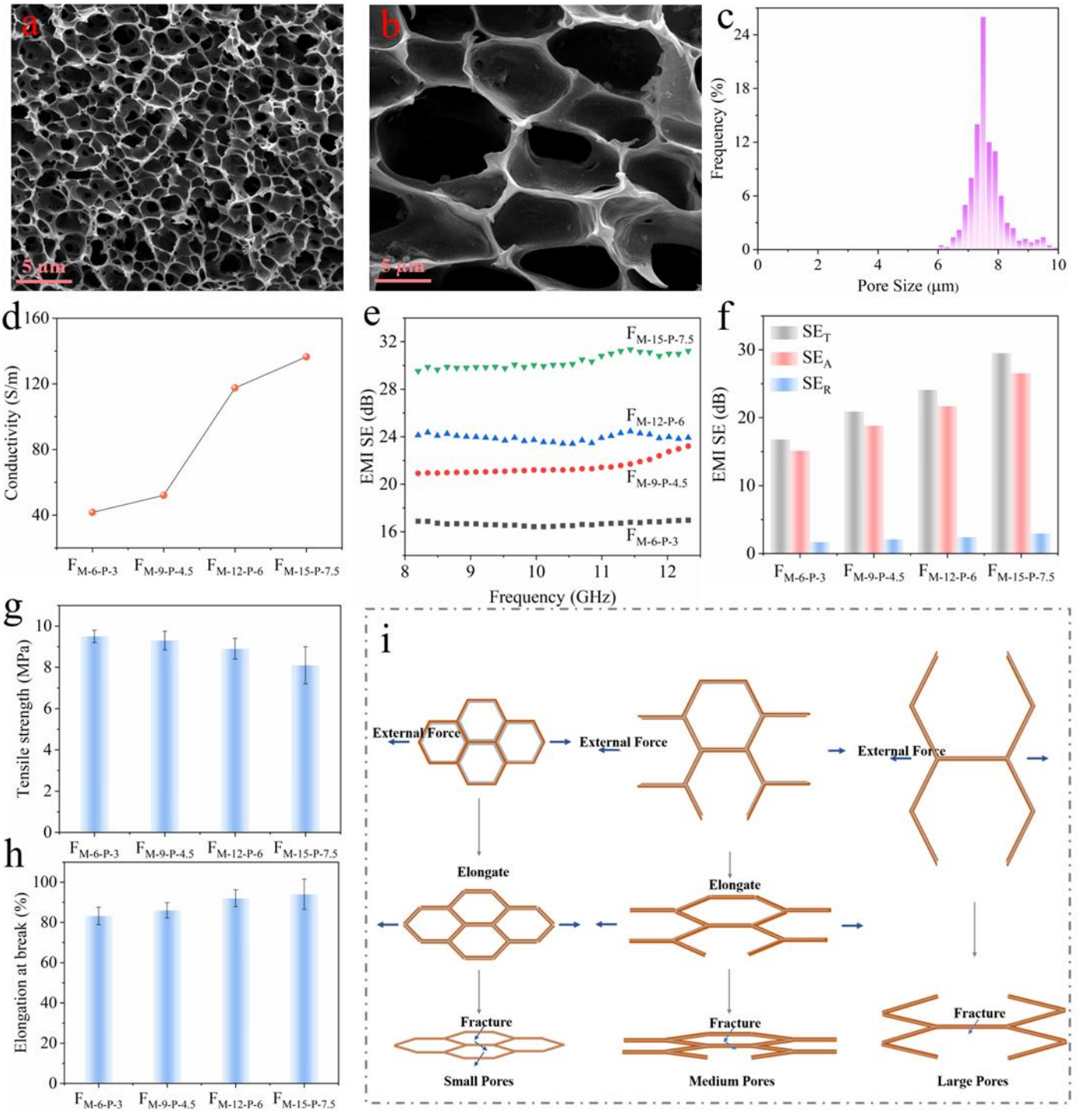

Fig. 5: (a) SEM images of the cross-section morphology of $F_{M-2b-P-b}$. (a) $F_{M-6-P-3}$; (b)$F_{M-15-P-7.5}$; (c) The pore size percentage of $F_{M-15-P-7.5}$; (d) Electrical conductivity of $F_{M-2b-P-b;}$ (e) The electromagnetic shielding performance of $F_{M-2b-P-b}$ as a function of frequency; (f) The values of the electromagnetic shielding parameters of $F_{M-2b-P-b}$; Mechanical properties of polyarylethernitrile porous film $F_{M-2b-P-b}$. (g) Tensile strength ; (h) Elongation at break; (i) The schematic diagram for fracture mechanism of $F_{M-2b-P-b}$.

$_b$ changes with the change of PVP K30 content, which results from the distribution of CNTs in the pores and the change of pore structure.

Fig. 4g and S5 is the tensile strength and elongation at break of $F_{M-12-P-b}$ prepared by PVP K30 with different contents when CNTs content is 12 wt%. The results showed that when the CNTs content was fixed at 12 wt%, the tensile strength and elongation at break of $F_{M-12-P-b}$ increased first and then decreased with the increase of PVP K30 content from 2 wt% to 8 wt%. When PVP K30 content increased from 2 wt% to 6 wt%, the tensile strength of $F_{M-12-P-b}$ increased from 3.7 MPa of $F_{M-12-P-2}$ to 8.9 MPa of $F_{M-12-P-6}$, and the elongation at break increased from 31.6 % of $F_{M-12-P-2}$ to 92.3 % of $F_{M-12-P-6}$. When the content of PVP K30 continued to increase to 8 wt%, the tensile strength of $F_{M-12-P-b}$ decreased to 8.2 MPa of $F_{M-12-P-8}$, and the elongation at break decreased to 87.5 % of $F_{M-12-P-8}$.

The change of mechanical properties of polyarylether nitrile porous film $F_{M\text{-}12\text{-}P\text{-}b}$ is mainly due to the change of honeycomb pore structure and CNTs distribution of $F_{M\text{-}12\text{-}P\text{-}b}$.

Fig. 5a, 5b, S6 and 5c is the SEM image of the cross-section morphology of $F_{M\text{-}2b\text{-}P\text{-}b}$ and pore size percentage of $F_{M\text{-}15\text{-}P\text{-}7.5}$ when the ratio of CNTs to PVP K30 is fixed at 2:1. The honeycomb pore wall in $F_{M\text{-}2b\text{-}P\text{-}b}$ was enriched with a single dispersed unentangled CNTs. CNTs overlapped with each other, and CNTs showed a spider-like enrichment on the entire honeycomb pore wall. There was no cluster-like CNTs agglomerated in the honeycomb pores and the nodes between the honeycomb pores, and no satin-like CNTs wrapped or interspersed in the pore wall. With the increase of CNTs concentration, the thickness of CNTs layer enriched on the honeycomb pore wall increases, which is the inevitable result of the increase of CNTs concentration. In addition, another obvious result is that the size of the honeycomb pores in the $F_{M\text{-}2b\text{-}P\text{-}b}$ section gradually increases with the increase of CNTs concentration. The average diameters of the honeycomb pores of $F_{M\text{-}6\text{-}P\text{-}3}$, $F_{M\text{-}9\text{-}P\text{-}4.5}$, $F_{M\text{-}12\text{-}P\text{-}6}$ and $F_{M\text{-}15\text{-}P\text{-}7.5}$ were 2.0 μm, 2.2 μm, 5.3 μm and 7.6 μm, respectively. This is mainly due to the promotion effect of PVP K30 on the increase of mass transfer rate is greater than the inhibition effect of CNTs concentration on the mass transfer rate.

Fig. 5d shows the conductivity of $F_{M\text{-}2b\text{-}P\text{-}b}$ prepared with different contents (CNTs/PVP K30=2). When CNTs/PVP K30=2 and the concentration of CNTs increased from 6 wt% to 15 wt%, the conductivity of the porous film $F_{M\text{-}2b\text{-}P\text{-}b}$ increased from 41.7 S/m of $F_{M\text{-}6\text{-}P\text{-}3}$ to 136.4 S/m of $F_{M\text{-}15\text{-}P\text{-}7.5}$. The gradual increase of conductivity is mainly due to the gradual increase of CNTs concentration. The above results show that when CNTs/PVP K30=2, CNTs are uniformly enriched in the honeycomb pores and an effective conductive pathway is formed. The change of honeycomb pore size caused by PVP K30 content has little effect on the conductivity of $F_{M\text{-}2b\text{-}P\text{-}b}$. Fig. 5e is the frequency dependence of the electromagnetic shielding performance of $F_{M\text{-}2b\text{-}P\text{-}b}$. It can be seen from the figure that the electromagnetic shielding performance of $F_{M\text{-}2b\text{-}P\text{-}b}$ hardly changes with the change of frequency. As the frequency increases from 8.2 GHz to 12.4 GHz, the electromagnetic shielding performance of $F_{M\text{-}2b\text{-}P\text{-}b}$ does not exceed 3 dB, indicating that $F_{M\text{-}2b\text{-}P\text{-}b}$ has stable electromagnetic shielding performance.

When CNTs/PVP K30=2 and the concentration of CNTs increased from 6 wt% to 15 wt%, the electromagnetic shielding performance of $F_{M\text{-}2b\text{-}P\text{-}b}$ at 8.2 GHz increased from 16.8 dB of $F_{M\text{-}6\text{-}P\text{-}3}$ to 29.5 dB of $F_{M\text{-}15\text{-}P\text{-}7.5}$. The increase of electromagnetic shielding performance is mainly caused by the gradual increase of the content of conductive CNTs. The electromagnetic shielding properties of $F_{M\text{-}9\text{-}P\text{-}4.5}$, $F_{M\text{-}12\text{-}P\text{-}6}$ and $F_{M\text{-}15\text{-}P\text{-}7.5}$ in the X-band are all greater than 20 dB, which meets the requirements of practical performance. The improved electromagnetic shielding performance of $F_{M\text{-}2b\text{-}P\text{-}b}$ is due to the uniform dispersion of CNTs on the honeycomb pore wall and the effective conductive network path constructed by the mutual overlap between CNTs. Since the conductive network presents a honeycomb structure, electromagnetic waves are reflected back and forth in the honeycomb conductive network structure, which is helpful to realize the effective dissipation of electromagnetic waves.

Fig. 5f shows the electromagnetic shielding parameters of $F_{M\text{-}2b\text{-}P\text{-}b}$ prepared with different contents. The results show that the absorption shielding SE_A of all $F_{M\text{-}2b\text{-}P\text{-}b}$ is greater than the reflection shielding SE_R, indicating that the $F_{M\text{-}2b\text{-}P\text{-}b}$ with a honeycomb conductive network structure is an electromagnetic shielding mechanism based on the absorption mechanism. With the increase of CNTs content from 6 wt% to 15 wt%, SE_T, SE_A and SE_R of $F_{M\text{-}2b\text{-}P\text{-}b}$ showed an upward trend, SE_T increased from 16.8 dB of $F_{M\text{-}6\text{-}P\text{-}3}$ to 29.6 dB of $F_{M\text{-}15\text{-}P\text{-}7.5}$, SE_A increased from 15.3 dB of $F_{M\text{-}6\text{-}P\text{-}3}$ to 26.5 dB of $F_{M\text{-}15\text{-}P\text{-}7.5}$, SE_R increased from 1.5 dB of $F_{M\text{-}6\text{-}P\text{-}3}$ to 3.1 dB of $F_{M\text{-}15\text{-}P\text{-}7.5}$. The increase of electromagnetic shielding parameter values of $F_{M\text{-}2b\text{-}P\text{-}b}$ can be attributed to the sawtooth reflection mechanism caused by the honeycomb pore wall of CNTs enriched in $F_{M\text{-}2b\text{-}P\text{-}b}$.

Fig. 5g and 5h show the tensile strength and elongation at break of $F_{M\text{-}2b\text{-}P\text{-}b}$ prepared with different contents (CNTs/PVP K30=2). The results show that when CNTs/PVP K30=2, with the increase of CNTs content from 6 wt% to 15 wt%, the tensile strength of $F_{M\text{-}2b\text{-}P\text{-}b}$ decreases gradually and the elongation at break increases gradually. The tensile strength of $F_{M\text{-}2b\text{-}P\text{-}b}$ decreased from 9.5 MPa of $F_{M\text{-}6\text{-}P\text{-}3}$ to 8.1 MPa of $F_{M\text{-}15\text{-}P\text{-}7.5}$, and the elongation at break increased from 83.2% of $F_{M\text{-}6\text{-}P\text{-}3}$ to 94.5% of $F_{M\text{-}15\text{-}P\text{-}7.5}$. Because CNTs in $F_{M\text{-}2b\text{-}P\text{-}b}$ are uniformly dispersed in the honeycomb pore wall, the change of mechanical properties is mainly due to the change of CNTs content and the honeycomb pore structure of $F_{M\text{-}2b\text{-}P\text{-}b}$. As shown in Fig. 5i, the increase of honeycomb pore size of porous film will lead to a decrease in the number of nodes that transmit stress and an increase in deformation space, so the tensile strength of $F_{M\text{-}2b\text{-}P\text{-}b}$ decreases and the elongation at break increases.

4. Conclusion

In this paper, the hydrophilic dispersing effect of PVP K30 was utilized to drive the migration of CNTs during the phase inversion formation process, and PEN porous films with enriched CNTs at the interface was prepared. Controlling the mass ratio of PVP K30 to CNTs effectively modulates the honeycomb pore structure, mitigating the undesirable agglomeration caused by high CNTs content. This promotes uniform CNTs accumulation within the pore walls of PEN porous film, reducing the CNTs content required to construct a continuous conductive network. Thanks to the synergistic effect of the uniformly enriched CNTs on the pore wall and the

adjustable honeycomb pore structure, the honeycomb conductive network structure of the interface-enriched CNTs is conducive to multiple reflections and absorption of electromagnetic waves inside the PEN porous films, resulting in effective attenuation of electromagnetic waves. When the CNTs content is 12 wt% and the honeycomb pore size is 6 μm, the total shielding performance of PEN porous films at 8.2 GHz is 26.5 dB, and the absorption efficiency is 23.6 dB. In addition, the tensile strength of PEN porous films is increased to 9.6 MPa, and the elongation at break is increased to 104%.

Acknowledgments

The financial support from Ministry of Science and Technology, China (MOST 2024YFB4006704), National Natural Science Foundation of China (No. 52503109), Natural Science Foundation of Shaanxi Province (2024-JC-YBQN-0140), Postdoctoral Program of Shaanxi Province (2023BSHEDZZ249) and Key R&D Program Projects in Shaanxi Province (2023JBGS-22) are gratefully acknowledged.

Conflict of Interest

The authors declare no conflict of interest.

Supporting Information

Applicable.

CRediT Statement

Lingling Wang: Methodology, Formal analysis, Investigation, Visualization and Writing - Original draft. **Xiaofei Zhao:** Software, Methodology, Writing - Review & editing. **Yue Yu:** Data Curation, Validation and Writing - Review & editing. **Xiufu Hua:** Conceptualization, Resources, Writing - Review & editing and Funding acquisition. **Renbo Wei:** Conceptualization, Project administration, Resources, Writing - Review & editing and Funding acquisition.

References

[1] J. Liu, V. Nicolosi, Electrically insulating electromagnetic interference shielding materials: a perspective, *Advanced Functional Materials*, 2025, **35**, 2407439, doi: 10.1002/adfm.202407439.

[2] C. Li, L. Qi, J. Fei, J. Yan, Z. Wu, T. Zhang, H. Li, Construction of polydopamine functionalized porous carbon network structure in polymer composites for excellent mechanical and electromagnetic interference shielding properties, *Carbon*, 2024, **217**, 118620, doi: 10.1016/j.carbon.2023.118620.

[3] T. Wu, L. Liang, Y. Bai, X. Mei, J. Jiao, Y. Ma, G. Wang, S. Zhang, Fabrication of corrosion-resistant and heat-resistant multi-walled carbon nanotubes/poly ether ether ketone/thermoplastic polyimide electromagnetic shielding foams based on double percolation structure, *Carbon*, 2023, **215**, 118423, doi: 10.1016/j.carbon.2023.118423.

[4] J. Xu, J. Fang, P. Zuo, Y. Wang, Q. Zhuang, Competitively assembled aramid-MXene Janus aerogel film exhibiting concurrently robust shielding and effective anti-reflection performance, *Advanced Functional Materials*, 2024, **34**, 2400732, doi: 10.1002/adfm.202400732.

[5] W. Liang, J. Wu, S. Zhang, P.-Y. Zhao, Y. Cong, Y. Guo, G.-S. Wang, Porous $Ti_3C_2T_x$ MXene nanosheets sandwiched between polyimide fiber mats for electromagnetic interference shielding, *Nano Research*, 2024, **17**, 2070-2078, doi: 10.1007/s12274-023-6405-4.

[6] R. B. Jagadeesh Chandra, B. Shivamurthy, S. B. Bore Gowda, M. Sathish kumar, Flexible linear low-density polyethylene laminated aluminum and nickel foil composite tapes for electromagnetic interference shielding, *Engineered Science,* 2022, **21**, 777, doi:10.30919/es8d777.

[7] H. Zhang, J. Wan, R. Wu, Y. Chen, H. Yu, S. Shi, MXenes for electromagnetic interference shielding: insights from structural design, *Carbon*, 2024, **218**, 118716, doi: 10.1016/j.carbon.2023.118716.

[8] R. Wei, Q. Huo, K. Liu, A. Y. Elnaggar, S. M. El-Bahy, Z. M. El-Bahy, J. Ren, L. Wang, Z. Wu, Distributing fluorinated carbon nanotube on pore walls of polyarylene ether nitrile porous films for advanced electromagnetic interference shielding, *Advanced Composites and Hybrid Materials*, 2024, **7**, 196, doi: 10.1007/s42114-024-00998-0.

[9] F. Guo, Y. Wang, K. Xue, L. Liu, J. Li, Y. Huang, Epoxy composites with satisfactory thermal conductivity and electromagnetic shielding yet electrical insulation enabled by Al_2O_3 platelet-isolated MXene porous microsphere networks, *Composites Science and Technology*, 2024, **248**, 110425, doi: 10.1016/j.compscitech.2023.110425.

[10] J. Chen, Y.-L. Liu, D.-X. Sun, X.-D. Qi, J.-H. Yang, Y. Wang, Recent progress in structural design of graphene/polymer porous composites toward electromagnetic interference shielding application, *Chemical Engineering Journal*, 2024, **495**, 153586, doi: 10.1016/j.cej.2024.153586.

[11] F. Gao, L. Zhou, K. Liu, Z. Feng, Q. Huo, C. Yang, T. Zhang, Y. Mao, D. Li, L. Wang, X. Hua, R. Wei, Improving energy storage properties of polyarylene ether nitrile with coral-like $CaCu_3Ti_4O_{12}$ nanorods, *Chemical Engineering Journal*, 2024, **493**, 152830, doi: 10.1016/j.cej.2024.152830.

[12] L. Wang, L. Lang, W. Ren, Z. Yang, T. Gao, Z. Zhao, M. Kallel, Y. Liu, Electrically insulating composite films with excellent electromagnetic interference shielding performance

enabled by multilayer structure, *Engineered Science*, 2025, **34**, 1477, doi: 10.30919/es1477.

[13] D. Yao, Z. Tang, Z. Liang, L. Zhang, Q.-J. Sun, J. Fan, G. Zhong, Q.-X. Liu, Y.-P. Jiang, X.-G. Tang, V. A. L. Roy, J. Ouyang, Adhesive, multifunctional, and wearable electronics based on MXene-coated textile for personal heating systems, electromagnetic interference shielding, and pressure sensing, *Journal of Colloid and Interface Science*, 2023, **630**, 23-33, doi: 10.1016/j.jcis.2022.09.003.

[14] C. Xie, Y. Fang, Y. Chen, J. Liu, Z.-X. Guo, X. Hao, C. Li, X. Tuo, Aramid-based highly conductive composite films by incorporating graphene for electromagnetic interference shielding and Joule heating applications, *Composites Science and Technology*, 2023, **236**, 109992, doi: 10.1016/j.compscitech.2023.109992.

[15] L. Xing, Y. Chen, Y. Yang, C. He, T. Wu, H. Xia, K. Shen, G. Tong, W. Wu, Incorporation of Fe_xO_y nanoparticles into 3D interlinked porous carbon nanofiber networks to synergistically enhance the electrical insulation, electromagnetic wave absorbing/shielding performance and thermal conductivity, *Chemical Engineering Journal*, 2023, **469**, 143952, doi: 10.1016/j.cej.2023.143952.

[16] L. Wang, Z. Feng, Q. Hou, Z. Dang, Y. Yu, C. Yang, B. Tang, Q. Zhou, X. Hua, R. Wei, T. X. Liu, Quaternary ammonium salt functionalized copper phthalocyanine-graphene oxide hybrids for cocatalyst-free carbon dioxide cycloaddition, *Advanced Composites and Hybrid Materials*, 2024, **8**, 40, doi: 10.1007/s42114-024-01081-4.

[17] J. Ruan, Z. Chang, H. Rong, T. S. Alomar, D. Zhu, N. AlMasoud, Y. Liao, R. Zhao, X. Zhao, Y. Li, B. B. Xu, Z. Guo, Z. M. El-Bahy, H. Li, X. Zhang, S. Ge, High-conductivity nickel shells encapsulated wood-derived porous carbon for improved electromagnetic interference shielding, *Carbon*, 2023, **213**, 118208, doi: 10.1016/j.carbon.2023.118208.

[18] Y. Zhang, K. Ruan, K. Zhou, J. Gu, Controlled distributed $Ti_3C_2T_x$ hollow microspheres on thermally conductive polyimide composite films for excellent electromagnetic interference shielding, *Advanced Materials*, 2023, **35**, 2211642, doi: 10.1002/adma.202211642.

[19] X.-X. Wang, Q. Zheng, Y.-J. Zheng, M.-S. Cao, Green EMI shielding: Dielectric/magnetic "genes" and design philosophy, *Carbon*, 2023, **206**, 124-141, doi: 10.1016/j.carbon.2023.02.012.

[20] X. Tang, J. Luo, Z. Hu, S. Lu, X. Liu, S. Li, X. Zhao, Z. Zhang, Q. Lan, P. Ma, Z. Wang, T. Liu, Ultrathin, flexible, and oxidation-resistant MXene/graphene porous films for efficient electromagnetic interference shielding, *Nano Research*, 2023, **16**, 1755-1763, doi: 10.1007/s12274-022-4841-1.

[21] C. Tang, S. Zhang, J. Zhang, X. Zhang, Z. Hang, Y. Li, Z. Yang, Silicon carbide coated carbon nanotube porous sponge with super Elasticity, low Density, high thermal Resistivity, and synergistically enhanced electromagnetic interference shielding performances, *Chemical Engineering Journal*, 2023, **469**, 144011, doi: 10.1016/j.cej.2023.144011.

[22] C. Ma, T. Mai, P.-L. Wang, W.-Y. Guo, M.-G. Ma, Flexible MXene/nanocellulose composite aerogel film with cellular structure for electromagnetic interference shielding and photothermal conversion, *ACS Applied Materials & Interfaces*, 2023, **15**, 47425-47433, doi: 10.1021/acsami.3c12171.

[23] X. Shen, J.-K. Kim, Graphene and MXene-based porous structures for multifunctional electromagnetic interference shielding, *Nano Research*, 2023, **16**, 1387-1413, doi: 10.1007/s12274-022-4938-6.

[24] Y. Q. Guo, K. P. Ruan, G. S. Wang, J. W. Gu, Advances and mechanisms in polymer composites toward thermal conduction and electromagnetic wave absorption, *Science Bulletin*, 2023, **68**, 1195-1212.

[25] H. Cheng, Z. Lu, Q. Gao, Y. Zuo, B. S. C. L. Chian, X. Liu, Z. Guo, C. Liu, C. Shen, PVDF-Ni/PE-CNTs composite foams with co-continuous structure for electromagnetic interference shielding and photo-electro-thermal properties, *Engineered Science*, 2021, **16**, 331-340, doi: 10.30919/es8d518.

[26] Y. Liu, Y. Wang, N. Wu, M. Han, W. Liu, J. Liu, Z. Zeng, Diverse structural design strategies of MXene-based macrostructure for high-performance electromagnetic interference shielding, *Nano-Micro Letters*, 2023, **15**, 240, doi: 10.1007/s40820-023-01203-5.

[27] J. Liu, M.-Y. Yu, Z.-Z. Yu, V. Nicolosi, Design and advanced manufacturing of electromagnetic interference shielding materials, *Materials Today*, 2023, **66**, 245-272, doi: 10.1016/j.mattod.2023.03.022.

[28] R. Wei, K. Liu, Y. Liu, Z. Wang, Y. Jiao, Q. Huo, X. Hua, L. Wang, X. Wang, Controlled distribution of MXene on the pore walls of polyarylene ether nitrile porous films for absorption-dominated electromagnetic interference shielding materials, *Small*, 2025, **21**, 2407142, doi: 10.1002/smll.202407142.

[29] R. Wei, Z. Wang, Y. Jiao, Y. Liu, S. Bao, L. Wang, X. Hua, X. Wang, Enhancing dielectric energy storage properties of poly(arylene ether nitrile) *via* controlling the distribution of boron nitride nanosheets, *Advanced Functional Materials*, 2025, **n/a**, e19368, doi: 10.1002/adfm.202519368.

[30] L. Wang, R. Wei, Y. luo, C. Liu, X. Liu, D. Li, Construction of alternating multilayer films with stable absorption-dominated electromagnetic shielding performance and reinforced mechanical properties *via* interface engineering, *Composites Part A: Applied Science and Manufacturing*, 2024, **176**, 107862, doi: 10.1016/j.compositesa.2023.107862.

[31] H. Liu, Y. Yang, N. Tian, C. You, Y. Yang, Foam-structured carbon materials and composites for electromagnetic interference

shielding: Design principles and structural evolution, *Carbon*, 2024, **217**, 118608, doi: 10.1016/j.carbon.2023.118608.

[32] M. Li, H. Liao, J. Wang, Multifunctional composite with porous gradient structure for absorption-oriented ultrahigh electromagnetic interference shielding, *Composites Part A: Applied Science and Manufacturing*, 2023, **173**, 107637, doi: 10.1016/j.compositesa.2023.107637.

[33] Z. Cheng, R. Wang, Y. Wang, Y. Cao, Y. Shen, Y. Huang, Y. Chen, Recent advances in graphene aerogels as absorption-dominated electromagnetic interference shielding materials, *Carbon*, 2023, **205**, 112-137, doi: 10.1016/j.carbon.2023.01.032.

[34] F. Liu, Z. Wei, X. Hu, Y. Cai, Z. Chen, C. Yang, Y. Zhan, H. Xia, Asymmetric segregated network design of ultralight and thermal insulating polymer composite foams for green electromagnetic interference shielding, *Composites Communications*, 2023, **38**, 101492, doi: 10.1016/j.coco.2022.101492.

[35] H. Gui, X. Zhao, S. Zuo, W. Liu, C. Wang, P. Xu, Y. Ding, C. Yao, Carbonized syndiotactic polystyrene/carbon nanotube/MXene hybrid aerogels with egg-box structure: a platform for electromagnetic interference shielding and solar thermal energy management, *ACS Applied Materials & Interfaces*, 2023, **15**, 39740-39751, doi: 10.1021/acsami.3c08176.

[36] L. Lyu, J. Liu, H. Liu, C. Liu, Y. Lu, K. Sun, R. Fan, N. Wang, N. Lu, Z. Guo, E. K. Wujcik, An overview of electrically conductive polymer nanocomposites toward electromagnetic interference shielding, *Engineered Science*, 2018, **2**, 26-42, doi: 10.30919/es8d615.

[37] P. Sharma, K. Singh, A. Kumar, D. Kumar, H. Mudila, U. Rednam, P. E. Lokhande, R. Aepuru, A. Kumar, Probing morpho-thermal evaluation of in situ fabricated polyaniline/polypyrrole/carbon nanotube nanocomposites, *ES Energy & Environment*, 2024, **24** 1125, doi: 10.30919/esee1125.

[38] S. Biswas, A. Biswas, K. Sen, Graphene based hybrid nanocomposite materials as sustainable energy resource: synthesis to application as supercapacitors, *ES Chemistry and Sustainability*, 2025, **3**, 1581, doi: 10.30919/escs1581.

[39] Q. Yang, Y. Gao, T. Li, L. Ma, Q. Qi, T. Yang, F. Meng, Advances in carbon fiber-based electromagnetic shielding materials: Composition, structure, and application, *Carbon*, 2024, **226**, 119203, doi: 10.1016/j.carbon.2024.119203.

[40] J. Tang, T. Li, Q. Liu, J. Du, J. Li, Q. Qi, F. Meng, Flexible microwave absorbing fabrics woven by high-strength graphene-based hybrid fibers with broadband electromagnetic response, *Journal of Materials Science & Technology*, 2024, **200**, 93-103, doi: 10.1016/j.jmst.2024.03.007.

[41] J. Zhang, Q. Wang, X. Xue, M. Li, X. Sun, J. Zhao, W. Zhang, C. Lu, Waste flame-retardant polyurethane foam/ground tire rubber/carbon nanotubes composites with hierarchical segregated structures for high efficiency electromagnetic interference shielding, *Composites Part A: Applied Science and Manufacturing*, 2023, **169**, 107530, doi: 10.1016/j.compositesa.2023.107530.

[42] L. Lang, W. Ren, J. Men, X. Mao, Z. Yang, S. Zhang, L. Wang, Advances in electromagnetic interference shielding materials with low reflection, *Engineered Science*, 2025, **36**, 1640, doi: 10.30919/es1640.

[43] J. Lei, Z. Han, L. Xiang, D. Pan, H. Liu, C. Shen, The preparation of SiO_2/SWCNT@Ni composite film with sandwich structure and its excellent electromagnetic shielding and thermal insulation performances in extreme environment, *Advanced Composites and Hybrid Materials*, 2025, **8**, 204, doi: 10.1007/s42114-025-01235-y.

[44] R. Shao, G. Wang, J. Chai, G. Wang, G. Zhao, Flexible, reliable, and lightweight multiwalled carbon nanotube/polytetrafluoroethylene membranes with dual-nanofibrous structure for outstanding EMI shielding and multifunctional applications, *Small*, 2024, **20**, 2308992, doi: 10.1002/smll.202308992.

[45] E. Kasiri, H. Haddadi, A. Asfaram, Magnetic multiwalled carbon nanotubes with ion-imprinted polymer coating for precious metal (Ag+) recovery from aqueous solutions: isotherm, kinetic, and thermodynamic analysis, *ES Materials & Manufacturing*, 2025, **28**, 1524, doi: 10.30919/mm1524.

[46] Y. Sheng, C. Li, J. Wang, X. Xia, G. J. Weng, Y. Su, Multiscale modeling of thermal conductivity of hierarchical CNT-polymer nanocomposite system with progressive agglomeration, *Carbon*, 2023, **201**, 785-795, doi: 10.1016/j.carbon.2022.09.057.

[47] R. Wei, Y. Liu, F. Gao, Z. Feng, Q. Huo, K. Liu, Z. Zhang, X. Lei, L. Wang, Enhancing high-temperature energy storage performance of poly(arylene ether nitrile) hybrids synergistically *via* phthalonitrile modified boron nitride and carbon nanotube, *Advanced Composites and Hybrid Materials*, 2024, **7**, 50, doi: 10.1007/s42114-024-00860-3.

[48] C. Wang, Flexible and biocompatible polystyrene/multi-walled carbon nanotubes films with high permittivity and low loss, *ES Materials & Manufacturing*, 2022, **19**, 791, doi: 10.30919/esmm5f791.

[49] H. Jia, Y. Qiao, Y. Zhang, C. Liu, X. Jian, Excellent and effective interfacial transition layer with an organic/inorganic hybrid carbon nanotube network structure for basalt fiber reinforced high-performance thermoplastic composites, *Chemical Engineering Journal*, 2023, **465**, 142995, doi: 10.1016/j.cej.2023.142995.

[50] Z. Han, Y. Niu, X. Shi, D. Pan, H. Liu, H. Qiu, W. Chen, B. B. Xu, Z. M. El-Bahy, H. Hou, E. R. Elsharkawy, M. A. Amin, C. Liu, Z. Guo, MXene@c-MWCNT adhesive silica nanofiber

membranes enhancing electromagnetic interference shielding and thermal insulation performance in extreme environments, *Nano-Micro Letters*, 2024, **16**, 195, doi: 10.1007/s40820-024-01398-1.
[51] A. Uthaman, H. M. Lal, C. Li, G. Xian, S. Thomas, Mechanical and water uptake properties of epoxy nanocomposites with surfactant-modified functionalized multiwalled carbon nanotubes, *Nanomaterials*, 2021, **11**, 1234, doi: 10.3390/nano11051234.
[52] J. Im, Y. H. Jeong, M. C. Kim, D. Oh, J. Son, K. Hyun, B. Jeong, S. Hong, J. Lee, Wet spinning of multi-walled carbon nanotube fibers, *Carbon*, 2024, **216**, 118532, doi: 10.1016/j.carbon.2023.118532.
[53] M. Li, S. Yu, X. Fang, Z. Du, X. Ge, Highly homogeneous and stable single-walled carbon nanotubes dispersion modified by polyvinylpyrrolidone and alkanolamine in water, *RSC Advances*, 2024, **14**, 12947-12953, doi: 10.1039/d4ra01614a.
[54] Z. Zhang, L. Zhou, L. Wang, Q. Hao, X. Hua, R. Wei, Enhancing energy storage density of poly(arylene ether nitrile) *via* incorporating modified barium titanate nanorods and hot-stretching, *Nano Research*, 2024, **17**, 7574-7584, doi: 10.1007/s12274-024-6678-2.
[55] Y. Liu, B. Tang, Z. Wang, Y. Jiao, Q. Hou, Z. Dang, X. Hua, L. Wei, L. Wang, R. Wei, Enhanced dielectric performances of strontium barium titanate nanorod composites *via* improved interfacial compatibility, *Journal of Colloid and Interface Science*, 2025, **680**, 85-95, doi: 10.1016/j.jcis.2024.11.088.